Forced subduction initiation recorded in the sole and crust of the Semail ophiolite of Oman

Carl Guilmette[1]*; Matthijs Smit[2]; Douwe J.J. van Hinsbergen[3]; Derya Gürer[3]; Fernando Corfu[4]; Benoit Charette[5]; Marco Maffione[6]; Olivier Rabeau, Dany Savard[7]

[1] Département de Géologie et de Génie Géologique, Université Laval, Québec, QC, Canada
[2] PCIGR, Department of Earth, Ocean and Atmospheric Sciences, University of British Columbia, Vancouver, BC, Canada
[3] Department of Earth Sciences, Utrecht University, Utrecht, Netherlands
[4] Department of Geosciences and CEED, University of Oslo, Oslo, Norway
[5] Department of Earth and Environmental Sciences, University of Waterloo, Waterloo, ON, Canada
[6] School of Geography, Earth and Environmental Sciences, University of Birmingham, Birmingham, United Kingdom
[7] LabMaTer, Département de Génie Géologique, Université du Québec à Chicoutimi, Chicoutimi, QC, Canada
*corresponding author carl.guilmette@ggl.ulaval.ca

Subduction zones are unique to Earth and fundamental in its evolution, yet we still know little on the causes and mechanisms of their initiation. Numerical models suggest far-field forcing may cause subduction initiation at weak pre-existing structures, whereas inferences from modern subduction zones suggest initiation through spontaneous lithospheric gravitational collapse. Measuring the time lag between initial lower plate burial and incipient extension in the upper plate should prove diagnostic in characterizing the subduction initiation mode. In modern systems, rocks that directly recorded initial lower plate burial should be found at the subduction interface and are inaccessible. Here we investigate a fossil system, the archetypal Semail ophiolite of Oman, which expose both lower and upper plate relics of incipient subduction stages. We show that burial of the lower plate predated upper plate extension and formation of Semail oceanic crust by at least 8 Myr, using geochronology of lower and upper plate material. Such a time lag requires far-field forced subduction initiation and provides for the first time unequivocal, direct evidence for a subduction initiation mechanism in the geological record.

The sinking of cold lithosphere in the Earth's mantle along subduction zones is widely recognised as the main driving force for global plate tectonics[1]. Despite decades of research, the processes and mechanisms of subduction initiation remain controversial[2]. Two main conceptual end-member mechanisms considered are 'induced' and 'spontaneous' subduction initiation[2, 3] (Fig. 1). Induced subduction initiation (ISI) requires a period of forced convergence, presumably accommodated at a pre-existing favourably oriented weak structure, until subduction eventually becomes self-sustained[4, 5, 6]. Alternatively, gravitational instability across oceanic transform faults or passive continental margins has been proposed to trigger lithospheric collapse and spontaneous subduction initiation (SSI) without net plate convergence[3, 7]. Whether only one of ISI or SSI is the active subduction initiation mode on Earth, or both modes can be activated depending on the tectonic setting, is a matter of debate[2, 3]. A fundamental criterion that would discern between ISI and SSI is the time lag between initial lower plate burial and ensuing upper plate extension (Fig. 1). During SSI, area consumed by subduction must simultaneously be balanced by area gained through upper plate extension[7, 8]. In contrast, upper plate extension following ISI must be generated by the growing slab after a period of forced underthrusting[4, 5, 9], resulting in a time lag of several millions of years. Constraining the magnitude of this time lag requires specific geochronological methods applied to a rock record of both the formation of the incipient subduction thrust and the onset of upper plate extension.

Models for subduction initiation are based on studies of earliest extension and magmatism in the forearc of modern subductions like the Izu-Bonin-Marianna system[7, 10], where rocks that directly recorded formation of the subduction interface are not exposed. Subduction initiation is widely assumed to have been spontaneous in this system[7, 8, 11]. Accordingly, the causes and consequences of subduction initiation are sought for in the tectonic setting at the time of forearc extension[12]. To date, the early subduction initiation history remains elusive[2], and an induced subduction initiation may have begun millions of years before forearc extension.

Research on supra-subduction zone (SSZ) ophiolites and associated metamorphic soles may yield more comprehensive insights into subduction initiation, because these provide a rock record of both upper plate extension and lower plate burial[2], respectively. SSZ ophiolites[13, 14] are interpreted as relic forearc oceanic lithosphere—similar in composition to the Izu-Bonin-Marianna forearc—that formed during subduction initiation[7, 8, 9] and was subsequently uplifted above sea level[15]. Many SSZ ophiolites rest on thin (< 500m) sheets of metamorphosed oceanic crust termed metamorphic soles. These metamorphic soles derive from the uppermost crust of the subducting lower plate[16, 17, 18, 19] that was preserved from further subduction by "welding" to the mantle section of the upper plate during subduction zone infancy[20, 21]. Garnet-clinopyroxene amphibolites found at the top of many metamorphic soles indicate high-pressure granulite facies[22, 23] peak metamorphic conditions (11-13 kbar and 850 °C). Metamorphism of oceanic crust to such conditions requires subduction along an anomalously hot geothermal gradient that is restricted to the initiation stage of a subduction zone[20, 21, 24]. These amphibolites likely represent the leading edge of the nascent slab and may therefore have directly recorded the initial burial of the lower plate during nucleation of a subduction interface[18, 20, 21].

The age of extension and crustal accretion in ophiolites is commonly estimated using U-Pb dating of zircon from gabbros and plagiogranites, interpreted to have formed in magma chambers below a spreading ridge[25, 26]. Dating of the earliest history of the subduction interface requires estimating the age of prograde metamorphism in the garnet-clinopyroxene amphibolites of metamorphic soles. Previous chronological studies of soles used $^{40}Ar/^{39}Ar$ hornblende or mica dating[9, 18, 20, 27, 28] and more recently U-Pb dating of zircons from melt segregations[29, 30]. These ages typically coincide or slightly postdate the ages of the magmatic crust of the overlying ophiolite[9, 18, 28]. Coinciding $^{40}Ar/^{39}Ar$ and U-Pb dates from sole rocks, and age data for ophiolitic crustal spreading have been taken to provide evidence for synchronous sole formation and upper plate spreading[28, 29]. The meaning of this coincidence in terms of sole formation is nevertheless debated[9]. Both methods date post-peak conditions rather than burial[31], and thus underestimate the age of sole formation by a yet unknown amount of time.

It is clear that rigorously constraining the chronology of subduction initiation requires new approaches in dating the earliest metamorphic minerals in soles. A promising technique is Lu-Hf dating of garnet, a petrological indicator of burial and heating in metamorphosed oceanic rocks. Owing to the robustness of the chronometer at high temperatures (900-950 °C)[32, 33, 34], prograde age records of garnet growth are typically well-preserved even in cases of long-lived supra-solidus conditions[35]. Here, we apply this approach to garnet from the metamorphic sole of the archetypal Semail ophiolite of Oman to date the early stages of sole development. The results, supported by textural observations and trace element mineral chemistry, are then combined with new U-Pb zircon and titanite data, and existing dates for the sole and overlying ophiolitic crust, to investigate the complete history of the sole, from burial and heating to exhumation and cooling. The comparison of garnet growth ages in the metamorphic sole and published extension ages in the overlying ophiolite constrains a minimum time lag between initial subducting plate burial and incipient upper plate extension.

The Semail Ophiolite

The Semail ophiolite (Fig. 2a) exposes over 20,000 km^2 of oceanic crust and upper mantle rocks underlain by a discontinuous thin sheet of metamorphic sole. The ophiolite-sole couple is thought to have been emplaced in Late Cretaceous time as a giant thrust sheet[36] over the Hawasina complex comprising distal oceanic rocks, and carbonates of the Arabian passive margin[37]. The Semail ophiolite exposes a section of oceanic lithosphere including residual upper mantle rocks made of harzburgite and dunite, plutonic lower and middle crust comprising cumulates and gabbros, and an upper crustal sheeted dike complex underlying pillowed to massive submarine basalts and abyssal sediments[38] (Fig. 2). High-precision U-Pb dating of the plutonic section across the ophiolite showed that the oceanic crust of the ophiolite was generated during rapid spreading between 96.1-95.5 Ma[25, 26].

The ophiolite has been classically interpreted as a relic fast spreading mid-ocean ridge[38, 39]. Recent evidence, however, clearly shows that the ophiolite formed above an active subduction zone[29, 40, 41]. Similarities in the chemostratigraphy of the Semail ophiolite and the Philippine Sea Plate forearc strengthened the inference that the ophiolite formed during subduction initiation[2, 13], either spontaneous[3, 8, 42] or induced[43, 44].

The sole of the Semail ophiolite comprises amphibolites that are notably garnet- and clinopyroxene-bearing near the contact with mantle rocks. Garnet-clinopyroxene sole amphibolites represent oceanic upper crustal MORB-like basaltic sequences[40] of unknown age, which were metamorphosed to peak conditions of 11-13 kbar and 850 °C[21, 45, 46]. U-Pb dating of zircon from melt segregations suggests solidification of the melt fraction by 96.16-94.82 Ma[26, 29, 30], followed by rapid cooling below the closure temperature of the $^{40}Ar/^{39}Ar$ system in hornblende (500-550°C) between 95.7 and 92.6 Ma[28]. The available data support the hypothesis that the upper crustal protolith of the sole was subducted to mantle depths in excess of 35 km along an incipient hot subduction plane before being transferred to the upper plate[20, 21].

This study focuses on two main Omani metamorphic sole localities: Wadi Tayin and Wadi Sumeini (Fig. 2). The Wadi Tayin locality[21, 45] (Fig. 2b) exposes amphibolites interlayered with thin quartz- and calc-silicate-rich layers, overlain by a middle quartzite dominated interval, and again an amphibolite layer with garnet amphibolites present in the top 5 m (Fig. 2e). The Sumeini sole locality[45, 46] (Fig. 2c) also exposes amphibolites, which become garnet- and clinopyroxene-bearing in the upper 10 m (Fig. 2d), whereas the lower section of the sole consists of epidote amphibolite with more abundant quartzite and marble. We collected samples WT-150 and WT-151 from the Wadi Tayin and SU-03A from the Sumeini sole localities (Figs. 2b, 2c, 2d, 2e) from garnet- and clinopyroxene-bearing amphibolites that occur as meter-scale coherent levels (Fig. 2d) or as boudins embedded in garnet-free amphibolite (Fig. 2e) immediately below the contact with the overlying mantle section.

Occurrence, composition and age of garnet, zircon and titanite

The samples show a hornblende-dominated nematoblastic fabric that wraps around boudinaged bands of garnet-clinopyroxene-rich granulite (Figs. 3a, 3b, 3c). Garnet occurs as subhedral cm-scale porphyroblasts with abundant inclusions (Fig. 3). Mineral compositions are consistent with those of similar samples used in previous petrological studies[21, 45, 46] and with high-pressure granulite facies metamorphic conditions[22, 23]. The strongly foliated matrix is defined by subhedral hornblende and subordinate anhedral diopside with abundant pseudomorphed anhedral plagioclase and fine-grained ilmenite-titanite symplectites. The granulite assemblage is variably overprinted by dynamic amphibolite-facies metamorphism. Sample SU-03A best preserves the granulite assemblage, whereas sample WT-150 shows the strongest amphibolite overprint. A lower-grade assemblage with epidote, prehnite and albite is found in fractures and veins, and as pseudomorphic replacements of plagioclase; the mafic minerals of the granulite assemblages are not substantially affected by such replacement.

Garnet shows complex zoning and inclusion patterns that differ between samples. Two garnet zones (grt-1 and grt-2) are nevertheless consistently observed. Grt-1 is defined by anhedral cores (grt-1) that are generally rich in Ca, Mn, and HREE (Figs. 3, 4). These cores are typically poikiloblastic with inclusions of titanite and apatite in innermost domains (grt-1a) and mono- and polymineralic inclusions of diopside, hornblende, plagioclase, ilmenite, titanite, and apatite in outer domains (grt-1b). Polymineralic inclusions locally show negative shapes and very low dihedral angles (Figs. 3f, 3g), suggesting they represent the solidification product of trapped melt. Grt-1a shows distinctly lower chondrite-normalised Gd/Yb than grt-1b. Grt-2 is defined by a textural and compositional mantle (grt-2) that encloses anhedral grt-1 cores. Grt-2 has fewer inclusions, is Mg-rich and Ca-poor, has high Gd_N/Yb_N, and shows strong and locally very well-defined oscillatory zoning for HREE (Fig. 4).

All three samples yielded garnet-whole rock Lu-Hf isochrons (Figs. 5a, 5b, 5c) with MSWD between 0.32 and 0.79, and uncertainties of 0.8 %RSD or better. The samples from Wadi Tayin yielded 104.1 ± 1.1 Ma (MSWD = 0.79; 150A) and 103.2 ± 1.2 Ma (MSWD = 0.32; 151A), and sample SU-03A from Sumeini provided 103.5 ± 1.6 Ma (MSWD = 0.62). All Lu-Hf age data are identical within uncertainty. Taking a weighted mean of these ages yields 103.7 ± 0.7 Ma (MSWD = 0.63), indicating no resolvable age scatter among the samples.

Zircon and titanite grains were recovered from sample WT-151. The zircon population consists largely of colourless, subequant and anhedral grains (Fig. 5d). Five analyses of such grains are clustered to the right of the Concordia curve. The slight discordance and spread in $^{207}Pb/^{235}U$ is a common feature of young zircon populations reflecting in part the likely bias in the decay constants used and initial ^{231}Pa excess[47]. All five $^{206}Pb/^{238}U$ ages overlap within error yielding a robust average age of 96.19 ± 0.14 Ma for crystallization of zircon. A fraction of four titanite grains provides a $^{206}Pb/^{238}U$ age of 95.60 ± 0.27 Ma.

Garnet growth in the Omani ophiolite soles

The microtextures and major and trace element distributions described above indicate the following growth history (Fig. 6). Grt-1 nucleated and initially grew at subsolidus conditions in the titanite stability field. The transition from grt-1a to grt-1b marks the prograde stabilization of ilmenite and the formation of inclusions indicative of the first occurrence of melt. Peritectic garnet growth at those conditions is further supported by evidence of melt segregations at the outcrop scale[29, 30] and by phase equilibria modelling[21, 23]. The distinct increase in Gd_N/Yb_N could relate to the dehydration melting of hornblende or to titanite break-down. Grt-2 represents peritectic garnet as indicated by its oscillatory zoning. This zoning is interpreted to reflect the competition between the rates of HREE uptake by growing garnet and diffusive HREE supply within the melt. Such a garnet growth sequence is consistent with phase equilibria modelling and experiments for MORB-like protoliths that predict suprasolidus grt-2 growth[21, 23] from 9 kbar-650°C to 11 kbar-850°C across the titanite-ilmenite transition[48].

The robustness of the Lu-Hf geochronometer[33, 34] is largely governed by the low diffusivity of Hf[49]. Closure temperatures of diffusive Hf loss for the grains analyzed are at least 900 °C[33] and hence exceed peak temperatures that the Omani sole samples were subjected to. Lu is more mobile and modelled mechanisms of age skewing by diffusive Lu redistribution[49] must be considered. These, however, clearly are not applicable here. The dated samples show exceptional preservation of the fine growth zoning in the distributions of Lu, which precludes any significant diffusive homogenization of Lu after garnet growth. The dates, which were determined for bulk-grain garnet populations, therefore represent an estimate of the average age of garnet growth weighted according to Lu distribution. The Lu-Hf dates for all three samples are identical, yet show different Lu distributions. This shows that weighing of ages was insignificant. Our data are thus best explained by a single, fast garnet growth event at sub- to suprasolidus conditions from roughly 550°C and 8 kbar to peak conditions of 850°C and 11-13 kbar (Fig. 6). Zircon (96.19 ± 0.14 Ma) may have crystallized from late highly fractionated solidifying trapped melt[29, 31] when the rocks cooled from peak conditions to subsolidus conditions of 700°C. The U-Pb dates of titanite (95.60 ± 0.27 Ma) represent cooling below 650 - 600°C[31].

Implications for subduction initiation

Rheological studies indicate that the upper part of a subducting oceanic plate will be transferred to the upper plate when conditions of 850°C and 11-13 kbar are reached at the interface, forming a metamorphic sole[20, 21]. We now show that garnet growth in the sole under the Semail ophiolite occurred at 104 Ma. This age provides a timing for burial, decoupling from the lower plate, and transfer to the upper plate. Between 104 Ma and zircon crystallization at 96 Ma, the welded sole did not record any major perturbation, likely staying at supra-solidus peak conditions while underthrusting progressed. Around 96 Ma, extension in the upper plate leads to oceanic lithosphere accretion along a spreading centre. Dikes that would have intruded the sole at this stage would have been transposed and amphibolitized during the main amphibolite-facies deformation event that is retrograde in nature for the garnet-clinopyroxene section of soles[16, 20, 21]. From 96.2 to 94.8 Ma, zircon crystallized from the segregated melt fractions[29, 30] in the underlying metamorphic sole, marking cooling to subsolidus conditions[29, 31] from >850°C to <750°C. Cooling to 600-650°C[31] occurred ~0.5 Myr later as shown by our titanite U-Pb age, whereas cooling to ~550°C and below is constrained by $^{40}Ar/^{39}Ar$ between ~95.5 Ma to ~92 Ma[28]. The onset of cooling in the sole thus coincides with the formation of SSZ oceanic crust (96.12-95.50 Ma[25, 26]). In the Semail ophiolite, sole formation, or lower plate burial, started >8 Myr before upper plate extension occurred. The inference that underthrusting below the mantle section predated formation of the ophiolitic crust by at least 8 Myr confirms a SSZ origin for the Semail ophiolitic crust, settling the long discussion regarding its origin [29, 38, 39, 41, 50].

The Semail ophiolite, preserving a ~50 km wide forearc lithosphere[8] measured perpendicular to its spreading direction[38], is 8 Myr younger than the sole age, and thus does not preserve the crust of the pre-subduction initiation lithosphere. Therefore, we cannot conclude with certainty that this is the oldest SSZ crust that formed after subduction initiation. However, during SSZ spreading, the ridge must have moved away from the trench at half-spreading rate[9], which was >10cm/yr[25]. At these rates, if upper plate spreading had started even a million years earlier, the ophiolite should have been ~50-100 km wider than today to preserve the 96-95.5 Ma old crust, and it is not likely it ever was. We therefore conclude that the oldest crust of the Semail ophiolite formed at the onset of upper plate extension.

Garnet growth in the metamorphic sole at 104 Ma and onset of SSZ crustal accretion by 96 Ma constrains a >8 Myr time lag between initial lower plate burial and the onset of upper plate extension, implying a >8 Myr period of forced convergence prior to upper plate extension. This time lag constitutes the first direct evidence from the geological record for ISI. The far-field causes driving the forced convergence should be sought considering the pre-104 Ma plate configuration and evolution, not the 96 Ma syn-upper plate extension configuration.
Our new results imply that SSZ ophiolite formation is not unequivocal evidence for SSI, as often assumed for Semail and other large and well-preserved ophiolites[3, 8, 42]. In fact, SSZ ophiolite formation rather indicates the onset of upper plate extension, which does not date subduction initiation in ISI.

Both the magnitude of the time lag between initial lower plate burial and incipient upper plate extension, and the age of the onset of convergence convey critical, previously unavailable information on subduction initiation. The magnitude of the time lag should reflect the balance between forces driving and resisting upper plate extension, depending on the nature, geometry and kinematics of the intervening plates, as indicated by numerical models[2, 4, 5, 6]. Longer time lags could indicate a strong upper plate, a long subduction interface or a slow convergence rate. Models of ISI at transform faults involving a very young upper plate[4, 5, 6] predict time lags of the order of 5-10 Myr, corresponding very well to our results. Nonetheless, the tectonic setting that led to initiation of subduction and formation of the Semail ophiolite must be validated from the rock record, in the pre-104 Ma configuration. Accordingly, the absolute timing of initial lower plate burial is also of utmost importance. The plate configuration and kinematics in which new subduction zones were initiated in the geological past might have significantly predated the earliest expression of upper plate spreading represented by ophiolitic or modern forearc crust. Such new insights into subduction initiation processes open new avenues for reconceptualization of the initiation and processes of global plate tectonics.

Figure Captions

Figure 1 : Conceptual lithospheric sections representing a spontaneous vs. induced subduction initiation and illustrating the predicted time lag between initial lower plate burial and incipient upper plate extension.

Figure 2: Geological maps and sample locations and field relationships. A) Geological map of Oman, modified from Nicolas et al. 2000 and Rioux et al. 2016. B) and C) Geological maps and sample locations at Wadi Tayin and Sumeini, maps after Cowan et al. 2014. D) and E) field

relationships for samples SU-03 and WT-151. The scale bar on the peridotite outcrop of E) is 10 cm.

Figure 3: Petrography of the investigated samples. A), B) and C) are micro-XRF chemical maps of thin sections for samples SU-03A, WT-150 and WT-151. D) and E) are close ups. F) and G) are BSE images of a melt pseudomorph inclusion in garnet from SU-03A. H), I) and J) are EPMA chemical profiles (located of 3A, 3B and 3C) showing almandine (Alm), grossular (Gr), pyrope (Py) and spessartine (Sp) mole fractions and Mg# = $Mg^{2+}/(Mg^{2+} + Fe^{2+})$.

Figure 4: Trace element content of representative garnet from samples SU-03A, WT-150 and WT-151. A), C) and E) Lu maps, location of maps is shown in figure 3A, 3B and 3C. B), D) and F) REE profiles normalised to chondrites (Sun and McDonough, 1989). Location of spot analyses is shown in 3A, 3C and 3E.

Figure 5: Geochronological results. A), B) and C) isochrons for garnet and whole rock fractions of samples SU-03A, WT-150 and WT-151. Data is available in table 3. D) Concordia diagram for zircon and titanite of sample WT-151. Zircon grains under binocular in inset, blue grid is 1 x 1 mm. Data is available in table 4.

Figure 6: P-T-t evolution of the Semail metamorphic sole. Supra-solidus garnet growth ages are from this study. Zircon ages are from this study and from Rioux et al. 2016. Titanite ages are from this study. Hornblende ages are compiled in Soret et al. 2017. 10% partial melting isomodes and solidus for MORB-like protoliths are from Palin et al. 2016. Garnet-in boundary

and titanite-ilmenite transition are from Liu et al. 1996. I, II and III are lithospheric section diagrams synthesizing our results. In III, spreading ages are from Rioux et al. 2012; 2013. See text for explanations.

References

1. Lithgow-Bertelloni C. Driving Forces: Slab Pull, Ridge Push. In: Harff J, Meschede M, Petersen S, Thiede J (eds). *Encyclopedia of Marine Geosciences*. Springer Netherlands: Dordrecht, 2016, pp 193-196.

2. Stern RJ, Gerya T. Subduction initiation in nature and models: A review. *Tectonophysics* 2017.

3. Stern RJ. Subduction initiation; spontaneous and induced. *Earth and Planetary Science Letters* 2004, 226(3-4): 275-292.

4. Gurnis M, Hall C, Lavier L. Evolving force balance during incipient subduction. *Geochemistry, Geophysics, Geosystems - G (super 3)* 2004, 5(7).

5. Hall CE, Gurnis M, Sdrolias M, Lavier LL, Mueller RD. Catastrophic initiation of subduction following forced convergence across fracture zones. *Earth and Planetary Science Letters* 2003, 212(1-2): 15-30.

6. Leng W, Gurnis M, Asimow P. From basalts to boninites; the geodynamics of volcanic expression during induced subduction initiation. *Lithosphere* 2012, 4(6): 511-523.

7. Stern RJ, Bloomer SH. Subduction zone infancy; examples from the Eocene Izu-Bonin-Mariana and Jurassic California arcs. *Geological Society of America Bulletin* 1992, 104(12): 1621-1636.

8. Stern RJ, Reagan M, Ishizuka O, Ohara Y, Whattam S. To understand subduction initiation, study forearc crust; to understand forearc crust, study ophiolites. *Lithosphere* 2012, 4(6): 469-483.

9. van Hinsbergen DJ, Peters K, Maffione M, Spakman W, Guilmette C, Thieulot C*, et al.* Dynamics of intraoceanic subduction initiation: 2. Suprasubduction zone ophiolite formation and metamorphic sole exhumation in context of absolute plate motions. *Geochemistry, Geophysics, Geosystems* 2015, 16(6): 1771-1785.

10. Reagan MK, Pearce JA, Petronotis K, Almeev RR, Avery AJ, Carvallo C*, et al.* Subduction initiation and ophiolite crust; new insights from IODP drilling. *International Geology Review* 2017, 59(11-12): 1439-1450.

11. Arculus RJ, Ishizuka O, Bogus KA, Gurnis M, Hickey-Vargas R, Aljahdali MH*, et al.* A record of spontaneous subduction initiation in the Izu-Bonin-Mariana Arc. *Nature Geoscience* 2015, 8(9): 728-733.

12. Faccenna C, Becker TW, Lallemand S, Steinberger B. On the role of slab pull in the Cenozoic motion of the Pacific plate. *Geophysical Research Letters* 2012, 39(3): L03305.

13. Pearce JA, Lippard SJ, Roberts S. Characteristics and tectonic significance of supra-subduction zone ophiolites. *Geological Society Special Publications* 1984, 16: 74-94.

14. Dilek Y, Furnes H. Ophiolite genesis and global tectonics; geochemical and tectonic fingerprinting of ancient oceanic lithosphere. *Geological Society of America Bulletin* 2011, 123(3-4): 387-411.

15. Dewey JF. Ophiolite obduction. *Tectonophysics* 1976, 31(1): 93-120.

16. Jamieson RA. P-T paths from high temperature shear zones beneath ophiolites. *Journal of Metamorphic Geology* 1986, 4(1): 3-22.

17. Spray JG. Possible causes and consequences of upper mantle decoupling and ophiolite displacement. *Geological Society, London, Special Publications* 1984, 13(1): 255-268.

18. Wakabayashi J, Dilek Y. Spatial and temporal relationships between ophiolites and their metamorphic soles; a test of models of forearc ophiolite genesis. *Special Paper - Geological Society of America* 2000, 349: 53-64.

19. Williams H, Smyth WR. Metamorphic aureoles beneath ophiolite suites and alpine peridotites; tectonic implications with west Newfoundland examples. *American Journal of Science* 1973, 273(7): 594-621.

20. Agard P, Yamato P, Soret M, Prigent C, Guillot S, Plunder A*, et al.* Plate interface rheological switches during subduction infancy; control on slab penetration and metamorphic sole formation. *Earth and Planetary Science Letters* 2016, 451: 208-220.

21. Soret M, Agard P, Dubacq B, Plunder A, Yamato P. Petrological evidence for stepwise accretion of metamorphic soles during subduction infancy (Semail ophiolite, Oman and UAE). *Journal of Metamorphic Geology* 2017, 35(9): 1051-1080.

22. Pattison DRM. Petrogenetic significance of orthopyroxene-free garnet + clinopyroxene + plagioclase ± quartz-bearing metabasites with respect to the amphibolite and granulite facies. *Journal of Metamorphic Geology* 2003, 21(1): 21-34.

23. Palin RM, White RW, Green ECR, Diener JFA, Powell R, Holland TJB. High-grade metamorphism and partial melting of basic and intermediate rocks. *Journal of Metamorphic Geology* 2016, 34(9): 871-892.

24. Peacock SM, Rushmer T, Thompson AB. Partial melting of subducting oceanic crust. *Earth and Planetary Science Letters* 1994, 121(1-2): 227-244.

25. Rioux M, Bowring S, Kelemen P, Gordon S, Dudás F, Miller R. Rapid crustal accretion and magma assimilation in the Oman-U.A.E. ophiolite: High precision U-Pb zircon geochronology of the gabbroic crust. *Journal of Geophysical Research: Solid Earth* 2012, 117(B7): n/a-n/a.

26. Rioux M, Bowring S, Kelemen P, Gordon S, Miller R, Dudas F. Tectonic development of the Samail Ophiolite; high-precision U-Pb zircon geochronology and Sm-Nd isotopic constraints on crustal growth and emplacement. *Journal of Geophysical Research: Solid Earth* 2013, 118(5): 2085-2101.

27. Hacker BR. Rapid emplacement of young oceanic lithosphere; argon geochronology of the Oman Ophiolite. *Science* 1994, 265(5178): 1563-1565.

28. Hacker BR, Mosenfelder JL, Gnos E. Rapid emplacement of the Oman Ophiolite; thermal and geochronologic constraints. *Tectonics* 1996, 15(6): 1230-1247.

29. Rioux M, Garber J, Bauer A, Bowring S, Searle M, Kelemen P*, et al.* Synchronous formation of the metamorphic sole and igneous crust of the Semail Ophiolite; new constraints on the tectonic evolution during ophiolite formation from high-precision U-Pb zircon geochronology. *Earth and Planetary Science Letters* 2016, 451: 185-195.

30. Warren CJ, Parrish RR, Waters DJ, Searle MP. Dating the geologic history of Oman's Semail Ophiolite; insights from U/Pb geochronology. *Contributions to Mineralogy and Petrology* 2005, 150(4): 403-422.

31. Yakymchuk C, Clark C, White RW. Phase relations, reaction sequences and petrochronology. *Reviews in Mineralogy and Geochemistry* 2017, 83: 13-53.

32. Baxter EF, Scherer EE. Garnet geochronology; timekeeper of tectonometamorphic processes. *Elements* 2013, 9(6): 433-438.

33. Scherer EE, Cameron KL, Blichert-Toft J. Lu-Hf garnet geochronology; closure temperature relative to the Sm-Nd system and the effects of trace mineral inclusions. *Geochimica et Cosmochimica Acta* 2000, 64(19): 3413-3432.

34. Smit MA, Scherer EE, Mezger K. Lu-Hf and Sm-Nd garnet geochronology; chronometric closure and implications for dating petrological processes. *Earth and Planetary Science Letters* 2013, 381: 222-233.

35. Anczkiewicz R, Szczepański J, Mazur S, Storey C, Crowley Q, Villa IM*, et al.* Lu–Hf geochronology and trace element distribution in garnet: Implications for uplift and exhumation of ultra-high pressure granulites in the Sudetes, SW Poland. *Lithos* 2007, 95(3): 363-380.

36. Hacker BR, Gnos E. The conundrum of Samail; explaining the metamorphic history. *Tectonophysics* 1997, 279(1-4): 215-226.

37. Searle MP, Warren CJ, Waters DJ, Parrish RR. Structural evolution, metamorphism and restoration of the Arabian continental margin, Saih Hatat region, Oman Mountains. *Journal of Structural Geology* 2004, 26(3): 451-473.

38. Nicolas A, Boudier F, Ildefonse B, Ball E. Accretion of Oman and United Arab Emirates ophiolite – Discussion of a new structural map. *Marine Geophysical Researches* 2000, 21(3): 147-180.

39. Boudier F, Ceuleneer G, Nicolas A. Shear zones, thrusts and related magmatism in the Oman ophiolite: Initiation of thrusting on an oceanic ridge. *Tectonophysics* 1988, 151(1): 275-296.

40. Ishikawa T, Nagaishi K, Umino S. Boninitic volcanism in the Oman Ophiolite; implications for thermal condition during transition from spreading ridge to arc. *Geology (Boulder)* 2002, 30(10): 899-902.

41. MacLeod CJ, Lissenberg L, Bibby LE. “Moist MORB” axial magmatism in the Oman ophiolite: The evidence against a mid-ocean ridge origin. *Geology* 2013, 41(4): 459-462.

42. Whattam SA, Stern RJ. The "subduction initiation rule"; a key for linking ophiolites, intra-oceanic fore-arcs, and subduction initiation. *Contributions to Mineralogy and Petrology* 2011, 162(5): 1031-1045.

43. Agard P, Jolivet L, Vrielynck B, Burov E, Monié P. Plate acceleration: The obduction trigger? *Earth and Planetary Science Letters* 2007, 258(3): 428-441.

44. Duretz T, Agard P, Yamato P, Ducassou C, Burov EB, Gerya TV. Thermo-mechanical modeling of the obduction process based on the Oman Ophiolite case. *Gondwana Research* 2016, 32: 1-10.

45. Cowan RJ, Searle MP, Waters DJ. Structure of the metamorphic sole to the Oman Ophiolite, Sumeini Window and Wadi Tayyin; implications for ophiolite obduction processes. *Special Publication - Geological Society of London* 2014, 392: 155-175.

46. Gnos E. Peak metamorphic conditions of garnet amphibolites beneath the Semail Ophiolite; implications for an inverted pressure gradient. *International Geology Review* 1998, 40(4): 281-304.

47. Rioux M, Bowring S, Cheadle M, John B. Evidence for initial excess 231Pa in mid-ocean ridge zircons. *Chemical Geology* 2015, 397: 143-156.

48. Liu J, Bohlen SR, Ernst WG. Stability of hydrous phases in subducting oceanic crust. *Earth and Planetary Science Letters* 1996, 143(1-4): 161-171.

49. Bloch E, Ganguly J, Hervig R, Cheng W. 176Lu–176Hf geochronology of garnet I: experimental determination of the diffusion kinetics of Lu3+ and Hf4+ in garnet, closure temperatures and geochronological implications. *Contributions to Mineralogy and Petrology* 2015, 169(2): 12.

50. Ishikawa T, Fujisawa S, Nagaishi K, Masuda T. Trace element characteristics of the fluid liberated from amphibolite-facies slab; inference from the metamorphic sole beneath the Oman Ophiolite and implication for boninite genesis. *Earth and Planetary Science Letters* 2005, 240(2): 355-377.

All correspondence and requests for materials should be addressed to Carl Guilmette (carl.guilmette@ggl.ulaval.ca), the corresponding author.

Acknowledgements

The research was financially supported by the Natural Sciences and Engineering Research Council of Canada, Discovery Grant RGPIN-2014-05681 to CG and RGPIN-2015-04080 to M.A.S, and European Research Council Starting Grant 306810 (SINK) and NWO Vidi grant 864.11.004 to D.J.J.v.H. We thank Mohammed Al Battashi (Sultanate of Oman Ministry of

Commerce and Industry, Directorate General of Minerals) for permission to undertake field sampling in Oman.

Author contributions

C.G. generated the project, led field work, completed the petrological study and wrote the manuscript.

M.S. conducted the Lu-Hf analyses and contributed to writing the manuscript

D.V.H. participated in field work, contributed to the rationale and to writing the manuscript

D.G. and F.C. completed and treated the U-Pb geochronological analyses

B.C. participated in field work, prepared samples and analyzed samples and contributed to the rationale

M.M. organised and participated in field work

D.S. conducted and treated the LA-ICP analyses

We have no competing financial interests.

Methods

Representative thin sections for each sample were mapped using a Bruker M4 Tornado µ-XRF instrument at Université Laval (Figure 3a, 3b, 3c) equipped with two 60 mm^2 Silicon Drift Detectors, operating at 50 kv and 300 nA with a step size of 20 µm and a dwell time of 3 ms per pixel, to find garnet grain sections that intersected the core. These garnet grains were subjected to major-element quantitative point analysis along radial profiles using a Cameca SX-100 five sprectrometer electron probe microanalyzer at Université Laval. Analytical conditions were 15 kV, 20 nA with a counting time of 20 s on peaks and 10 s on background. Calibration standards used were generally simple oxides (GEO Standard Block of P&H Developments), or minerals where needed (Mineral Standard Mount MINM25-53 of Astimex Scientific Limited; reference samples from Jarosewich et al., 1980). Data were reduced using the PAP model. The data are available in Table 1 and figures 3h, 3i and 3j.

Trace-element analysis of the garnet sections was done by laser ablation inductively coupled plasma mass spectrometry (LA-ICP-MS) at LabMaTer (Université du Québec à Chicoutimi), using a RESOlution 193 nm excimer laser (Australian Scientific Instrument) and a S155 Laurin Technic ablation cell system coupled to an Agilent 7900 quadrupole ICP-MS. Spot analyses were conducted with a 33 µm beam operating at 15 Hz, 5 J/cm^2 in a 4ms/isotope cycle. High resolution mapping was done with a 20 µm beam at a speed of 80 µm/s (figures 4a, 4c and 4e) and pulsing of 30 Hz at $5J/cm^2$ in a 4 ms/isotope cycle. Calibrant used was the synthetic basalt glass GSE-1G (USGS), using preferred values from the GEOREM database (Jochum *et al.,* 2005). The data have been processed with IOLITE freeware (Paton *et al.,* 2011) to generate maps and achieve fully-quantitative results on spots analysis using ^{29}Si as internal standard. The data are available in Table 2 and figure 4.

For garnet Lu-Hf and zircon U-Pb geochronology, samples were disaggregated using an Electric Pulse Disaggregation instrument at Overburden Drilling Management Ltd to 90% <1mm. Bulk-rock powders were created from this fraction. Large garnet concentrates of 800 mg or more were extracted from the samples through standard concentration methods: sieving, magnetic separation using a Frantz magnetic barier separator, heavy liquor density separation and hand-picking on a binocular microscope. Zircon and titanite grains were handpicked from the heavy mineral fraction.

Garnet Lu-Hf chronology was done at the Pacific Centre for Isotopic and Geochemical Research, University of British Columbia. There, garnet crystals and bulk-rock powder were transferred to screw-top PFA vials and weighed. Garnet grains were then washed using de-ionized water and bathed in 1 N HCl at room temperature for 1 h. After removing the HCl, garnet samples were dried, mixed with a ^{176}Lu- ^{180}Hf isotope tracer that has a Lu/Hf similar to that of generic garnet, and digested through repeated addition of HF:HNO_3:$HClO_4$ and 6 N HCl, each step followed by evaporation to dryness. After admixing of a mixed ^{176}Lu- ^{180}Hf isotope tracer with low Lu/Hf, the bulk-rock powders were digested in a stainless-steel digestion vessel at 180 °C for 7 days using HF:HNO_3.

After digestion, all samples were dried down, re-dissolved in 6 N HCl, diluted to 3 N HCl using de-ionized H_2O, and centrifuged. The solution containing the garnet elemental solute was then loaded onto polypropylene columns containing a 1-ml Ln-Spec® resin bed and subjected to REE-HFSE chromatography modified from the method of Münker et al. (2001). Isotope analyses for Hf and Lu were done using the Nu Instruments *Plasma HR* multi-collector (MC) ICPMS at PCIGR. For Lu analyses, isobaric interference of ^{176}Yb on m/z corresponding to mass 176 was corrected using an exponential correlation between ^{176}Yb/^{171}Yb and ^{174}Yb/^{171}Yb. This correlation was calibrated through replicate analyses of Yb solution standards from the National Institute of Standards and Technology performed at different concentrations (10-100 ppb; Blichert-Toft et al., 2002). For Hf isotope analyses, ^{180}Ta and ^{180}W interferences were estimated on the basis of

$^{181}Ta/^{177}Hf$ and $^{183}W/^{177}Hf$, assuming natural abundance and a Hf-based mass bias. Mass bias was assumed to follow an exponential law and was corrected for applying $^{179}Hf/^{177}Hf = 0.7325$ (Hf, Ta, W) and $^{173}Yb/^{171}Yb = 1.1296$ (Lu, Yb). Any resolvable drift was corrected for assuming linear time dependence. Hafnium isotope ratios are reported relative to the JMC-475 Hf standard ($^{176}Hf/^{177}Hf = 0.28216$; Blichert-Toft et al., 1997). The external $^{176}Hf/^{177}Hf$ reproducibility (2 s.d.) of replicate JMC-475 analyses done at concentrations similar to those of sample solutions was 0.4 ε_{Hf} during the course of our analytical sessions. The external reproducibility of $^{176}Hf/^{177}Hf$ was estimated from the standard scatter at the given sample concentration and internal error. This estimate was made by comparing internal and external uncertainty for replicate analyses of JMC-475 done at concentrations that bracketed those of samples (10-50 ppb; Bizzarro et al., 2003). The Lu-Hf isochrons were established using *Isoplot* v. 3.27 (Ludwig, 2003) applying 1.876×10^{-11} yr^{-1} for $\lambda^{176}Lu$ (Scherer et al., 2001; Söderlund et al., 2004). All uncertainties are cited at the 2-s.d. level. The results are provided in Table 3 and Figure 5.

The samples were screened for zircon and titanite; both minerals were found only in sample 151A. After selection under an optical microscope zircon was subjected to chemical abrasion (Mattinson, 2005, 2010) whereas titanite was not abraded. The selected grains were then spiked with a ^{202}Pb-^{205}Pb-^{235}U tracer, followed by dissolution, chemical separation of Pb and U, and mass spectrometry, after the procedure detailed in Krogh, (1973) with modifications described in Corfu, (2004). The Pb measurements were done mostly with an ion counting secondary electron multiplier. The obtained data were corrected with fractionation factors determined from the 205Pb/202Pb ratio of the tracer (around 0.1%/amu for Pb) and 0.12%/amu for U, subtracting blanks of 0.1 pg U and 2 pg Pb, or less when the total common Pb was below that level. The remaining initial Pb was corrected using compositions calculated with the model of Stacey and Kramers, (1975). The data were also adjusted for a deficit of ^{206}Pb due to initial deficiency of ^{230}Th (Schärer, 1984) and the tracer was calibrated with reference to the ET100 solution (Condon, personal communication, 2014). Plotting and regressions were done with the Isoplot software package (Ludwig, 2009). The decay constants are those of Jaffey et al. (1971). The results are provided in Table 4 and figure 5.

The authors declare that all the data supporting the findings of this study are available within the paper and its supplementary information files.

References

Corfu, F. (2004). U--Pb age, setting and tectonic significance of the anorthosite--mangerite--charnockite--granite suite, Lofoten--Vesterålen, Norway. *Journal of Petrology*, *45*(9), 1799–1819.

Jaffey, A. H., Flynn, K. F., Glendenin, L. E., Bentley, W. C. t, & Essling, A. M. (1971). Precision measurement of half-lives and specific activities of U 235 and U 238. *Physical Review C*, *4*(5), 1889.

Jarosewich, E., Nelen, J.A., Norberg, J.A., 1980. Reference samples for electronmicroprobe analysis. Geostandards Newsletter 4, 43–47.

Jochum, K. P., Nohl, U., Herwig, K., Lammel, E., Stoll, B., & Hofmann, A. W. (2005). GeoReM: a new geochemical database for reference materials and isotopic standards. *Geostandards and Geoanalytical Research*, *29*(3), 333-338.

Krogh, T. E. (1973). A low-contamination method for hydrothermal decomposition of zircon and extraction of U and Pb for isotopic age determinations. *Geochimica et Cosmochimica Acta*, *37*(3), 485–494.

Krogh, T. E. (1982). Improved accuracy of U-Pb zircon ages by the creation of more concordant systems using an air abrasion technique. *Geochimica et Cosmochimica Acta*, *46*(4), 637–649.

Ludwig, K. R. (2009). Isoplot 4.1. A geochronological toolkit for Microsoft Excel. *Berkeley Geochronology Center Special Publication*, *4*, 76.

Mattinson, J. M. (2005). Zircon U--Pb chemical abrasion ("CA-TIMS") method: combined annealing and multi-step partial dissolution analysis for improved precision and accuracy of zircon ages. *Chemical Geology*, *220*(1), 47–66.

Mattinson, J. M. (2010). Analysis of the relative decay constants of 235 U and 238 U by multi-step CA-TIMS measurements of closed-system natural zircon samples. *Chemical Geology*, *275*(3), 186–198.

Paton, C., Hellstrom, J., Paul, B., Woodhead, J., & Hergt, J. (2011). Iolite: Freeware for the visualisation and processing of mass spectrometric data. *Journal of Analytical Atomic Spectrometry*, *26*(12), 2508-2518.

Schärer, U. (1984). The effect of initial 230 Th disequilibrium on young U Pb ages: the Makalu case, Himalaya. *Earth and Planetary Science Letters*, *67*(2), 191–204.

Stacey, J. S. t, & Kramers, 1JD. (1975). Approximation of terrestrial lead isotope evolution by a two-stage model. *Earth and Planetary Science Letters*, *26*(2), 207–221.

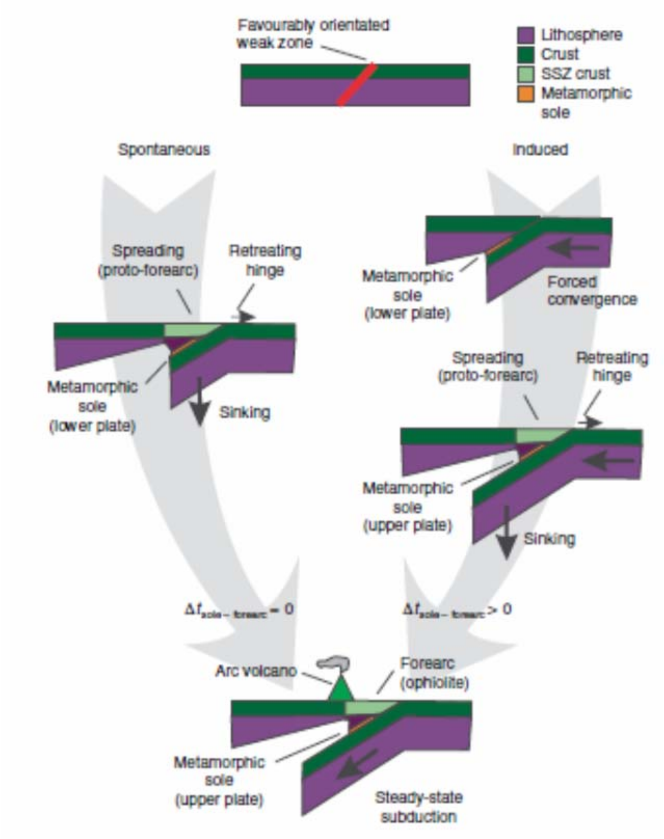

Fig. 1 | Conceptual lithospheric sections representing SSI versus ISI. The time lag between initial lower plate burial and incipient upper plate extension is diagnostic of the subduction initiation mode.

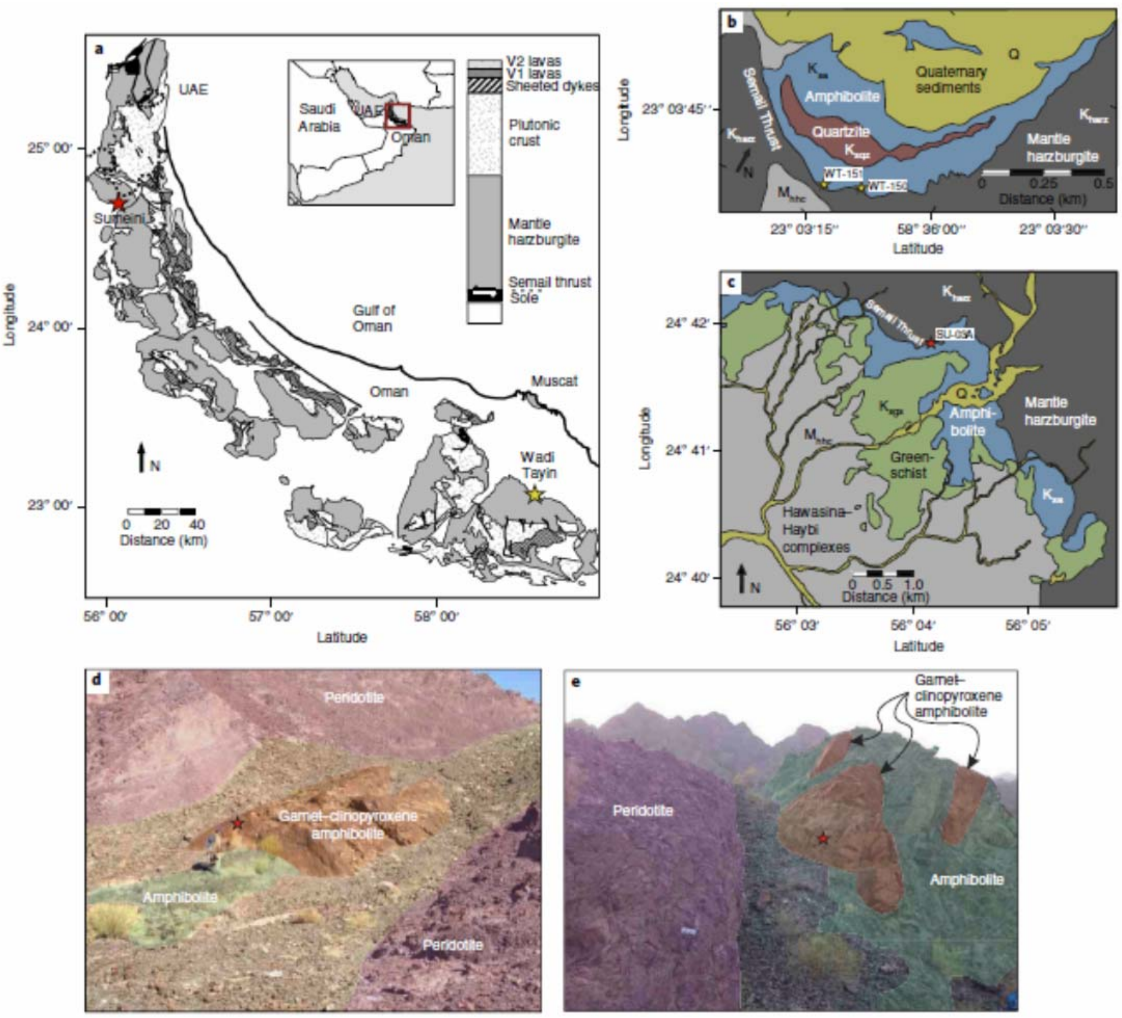

Fig. 2 | Geological maps, sample locations and field relationships. a, Geological map of Oman. **b**,**c**, Geological maps and sample locations at Wadi Tayin (**b**) and Sumeini (**c**). **d**,**e**, Field relationships for samples SU-03 (**d**) and WT-151 (**e**). Scale bar on the peridotite outcrop of **e**, 10 cm. Panels **a**–**c** adapted from ref. [29], Elsevier. Red stars are sampling sites. K_{harz}, Cretaceous harzburgite; K_{sqz}, Cretaceous sole – quartzite; K_{sa}, Cretaceous sole – amphibolite; K_{sgs}, Cretaceous sole – greenschist; Q, Quaternary; M_{hhc}, Hawasina and Haybi complexes.

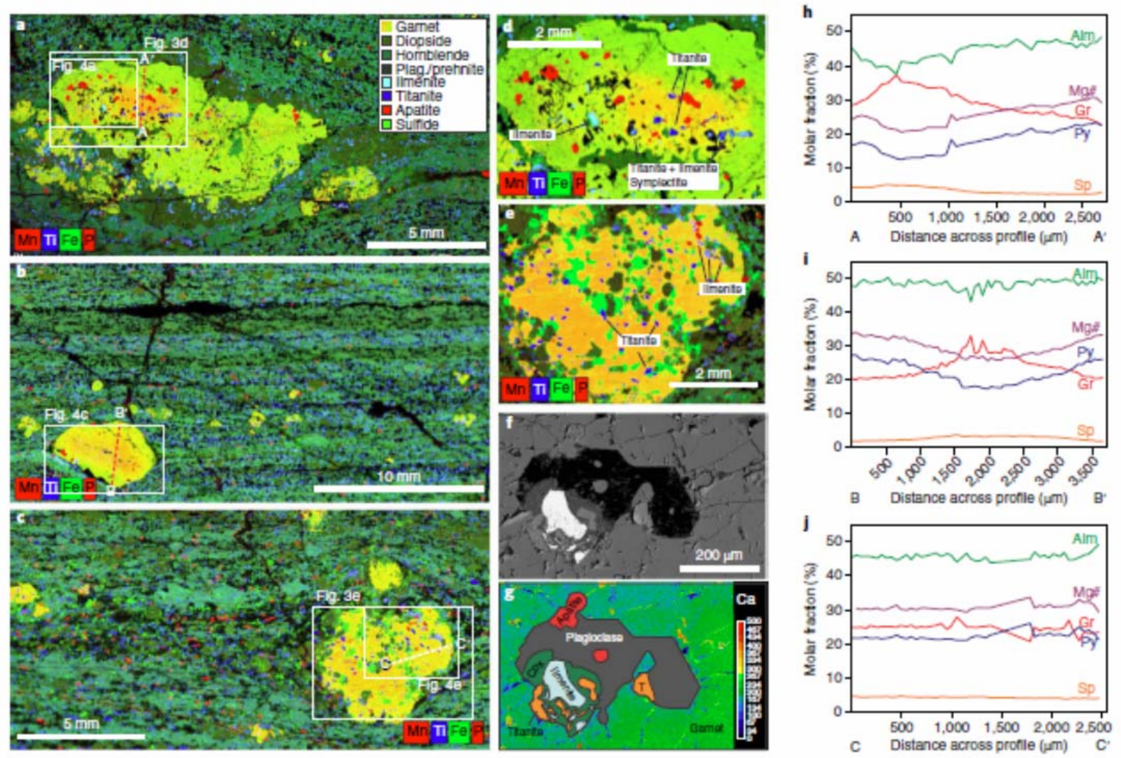

Fig. 3 | Petrography of the investigated samples. a–c, Micro-X-ray fluorescence chemical maps of thin sections for the samples SU-03A (**a**), WT-150 (**b**) and WT-151 (**c**). **d**, Magnified view of the solid boxed area in **a**. **e**, Magnified view of the solid boxed area in **c**. **f**,**g**, Back-scatter detector image (**f**) and composite Ca map + schematic (**g**) of a melt pseudomorph inclusion in garnet from SU-03A. The colour scale in garnet in **g** represents Ca relative abundance. **h–j**, Electron probe microanalyser chemical profiles for the samples SU-03A (**h**), WT-150 (**i**) and WT-151 (**j**), showing almandine (Alm), grossular (Gr), pyrope (Py) and spessartine (Sp) mole fractions and Mg# = $Mg^{2+}/(Mg^{2+} + Fe^{2+})$. The locations of the A–A′, B–B′ and C–C′ profiles in **h–j** are indicated by dashed lines in **a–c**, respectively. Plag., plagioclase; Cpx, clinopyroxene.

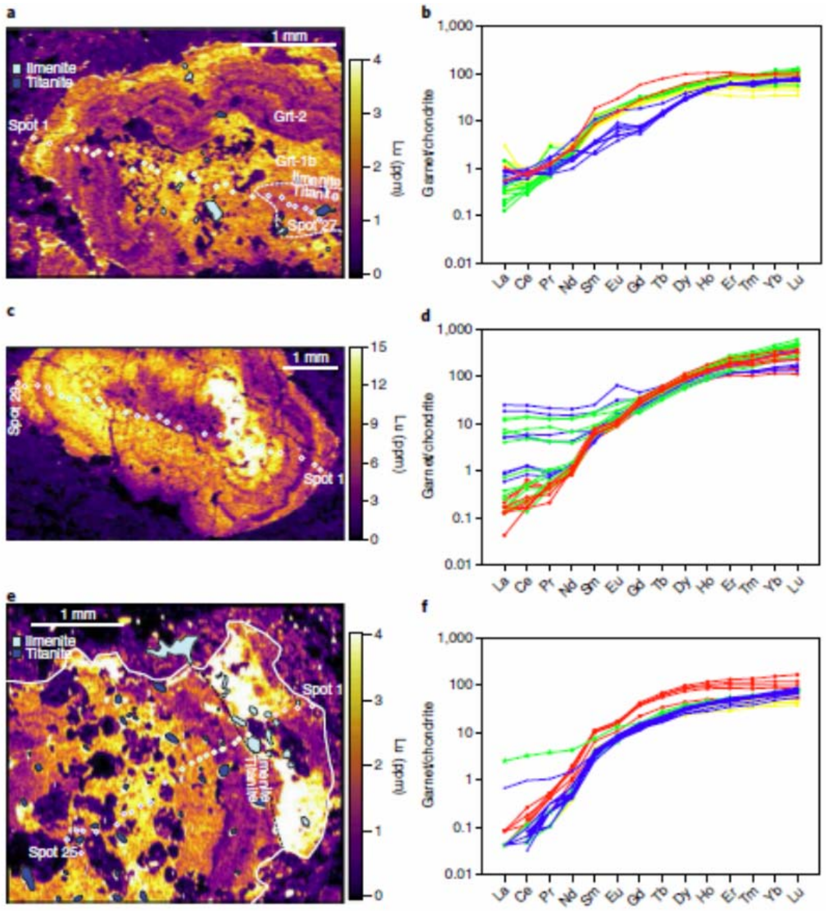

Fig. 4 | Trace element content of representative garnet from samples SU-03A, WT-150 and WT-151. a,c,e, Lutetium maps for SU-03A (**a**), WT-150 (**c**) and WT-151 (**e**), the locations of which are indicated by the dashed squares in Fig. 3a–c, respectively. **b,d,f**, Rare earth element (REE) profiles normalized to chondrites[51]. The locations of the spot analyses are shown **a**, **c** and **e**, respectively.

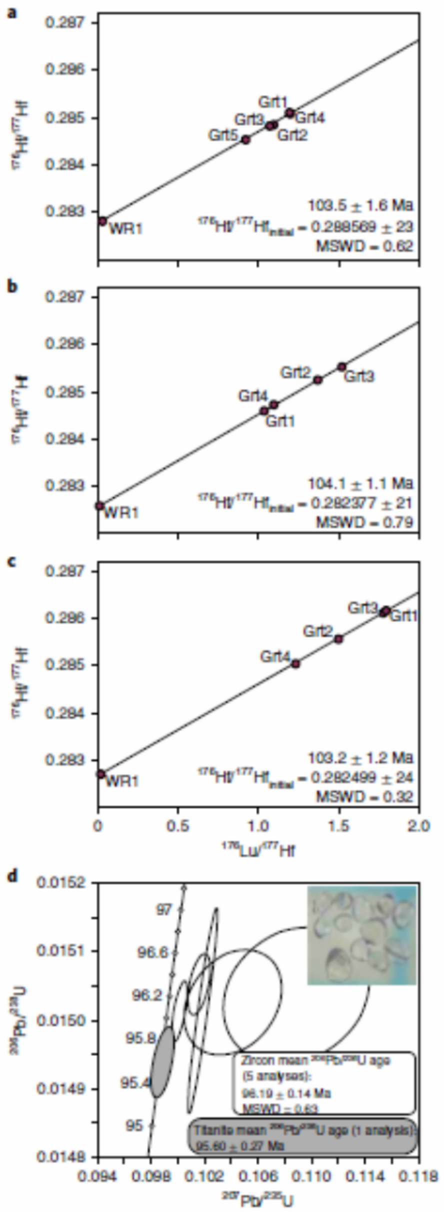

Fig. 5 | Geochronological results. a–c, Isochrons for garnet (Grt1–5) and whole rock (WR1) fractions of samples SU-03A (**a**), WT-150 (**b**) and WT-151 (**c**). Data are available in Supplementary Table 3. **d**, Concordia diagram for zircon and titanite of sample WT-151. Data point error elipses are 2σ. Inset, magnified image of zircon grains (1×1mm). Data are available in Supplementary Table 4.

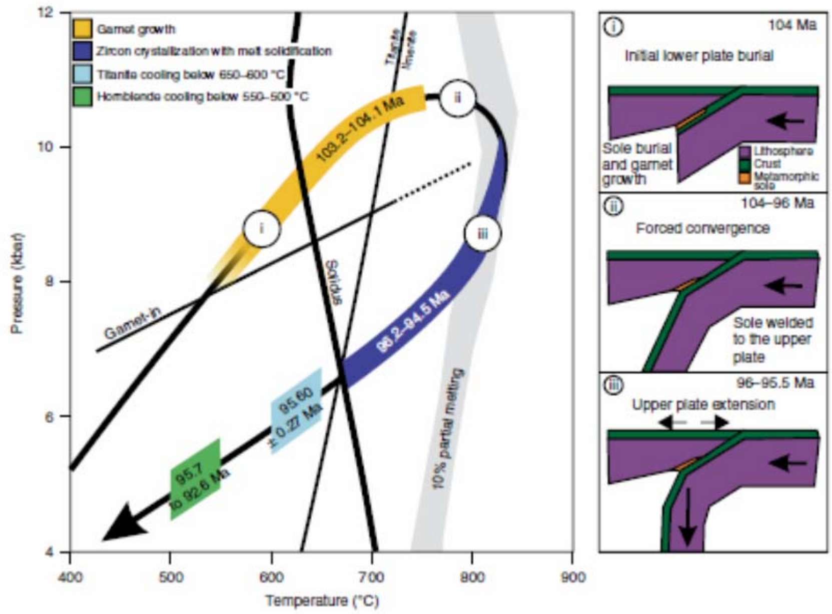

Fig. 6 | Pressure–temperature–time evolution of the Semail metamorphic sole. The pressure–temperature trajectory and hornblende ages are from Soret et al.[21]. The supra-solidus garnet growth ages and titanite ages are from this study. The zircon ages are from this study and Rioux et al.[29]. The 10% partial melting isomodes and solidus for MORB-like protoliths are from Palin et al.[23]. The garnet-in boundary and titanite–ilmenite transition are from Liu et al.[48]. i–iii, lithospheric section diagrams synthesizing our results. In iii, the spreading ages are from Rioux et al.[25,26]. See main text for details.

nature geoscience ARTICLES
https://doi.org/10.1038/s41561-018-0209-2

Forced subduction initiation recorded in the sole and crust of the Semail ophiolite, Oman

Supplementary information

Table 3 : Lu-Hf isotopic dilution analysis of garnet and whole fractions from the Semail metamorphic sole.

Sample	Aliquot	Lu (ppm)	Hf (ppm)	$^{176}Lu/^{177}Hf$	2SD	$^{176}Hf/^{177}Hf$	2SD	Lu-Hf age (Ma)	2SD	$^{176}Hf/^{177}Hf_{initial}$	2SD	MSWD
WT-150	Grt-1	4.06	0.554	1.038	0.003	0.284388	0.000036					
	Grt-2	5.35	0.553	1.371	0.003	0.285051	0.000035					
	Grt-3	4.88	0.454	1.523	0.004	0.285329	0.000027					
	Grt-4	5.52	0.714	1.096	0.003	0.284526	0.000028					
	WR-1	0.193	4.20	0.006516	0.000016	0.282388	0.000022					
								104.1	**1.1**	**0.282377**	**0.000021**	**0.79**
WT-151	Grt-1	4.81	0.380	1.794	0.004	0.285975	0.000056					
	Grt-2	5.01	0.475	1.495	0.004	0.285381	0.000047					
	Grt-3	5.08	0.405	1.777	0.004	0.285926	0.000053					
	Grt-4	4.97	0.573	1.231	0.003	0.284854	0.000049					
	WR-1	0.0888	1.20	0.01049	0.00003	0.282521	0.000025					
								103.2	**1.2**	**0.282499**	**0.000024**	**0.32**
SU-03	Grt-1	2.29	0.273	1.192	0.003	0.284910	0.000059					
	Grt-2	2.29	0.298	1.091	0.003	0.284652	0.000059					
	Grt-3	3.01	0.398	1.070	0.003	0.284635	0.000068					
	Grt-4	1.07	0.127	1.196	0.003	0.284886	0.000048					
	Grt-5	2.82	0.435	0.917	0.002	0.284336	0.000031					
	WR-1	0.565	2.97	0.02692	0.00007	0.282622	0.000023					
								103.5	**1.6**	**0.282569**	**0.000023**	**0.62**

Table 4 : U-Pb data for zircon and titanite of sample WT-151

Properties	Weight [ug]	U [ppm]	Th/U	Pbc [pg]	206/204	207/235	2 sigma [abs]	206/238	2 sigma [abs]	rho	207/206	2 sigma [abs]	206/238 [Ma]	2 sigma [abs]	207/235 [Ma]	2 sigma [abs]
(a)	(b)	(b)	(c)	(d)	(e)	(f)	(f)	(f, g)	(f)	(f)	(f,g)	(f)	(f,g)	(f)	(f)	(f)
Z eq [1]	10	17	0.46	1.9	102	0.10889	0.00447	0.015038	0.000082	0.19	0.05252	0.00212	96.22	0.52	104.95	4.09
Z eq [1]	25	73	0.01	0.8	2100	0.10185	0.00090	0.015011	0.000123	0.94	0.04921	0.00014	96.05	0.78	98.48	0.83
Z eq [1]	18	10	0.39	1.3	152	0.10411	0.00298	0.015027	0.000063	0.26	0.05025	0.00140	96.15	0.40	100.56	2.74
Z eq [3]	15	73	0.09	1.5	671	0.10164	0.00069	0.015054	0.000036	0.51	0.04897	0.00029	96.32	0.23	98.29	0.63
Z eq [2]	13	117	0.02	0.9	1558	0.10015	0.00046	0.015014	0.000036	0.68	0.04838	0.00017	96.07	0.23	96.92	0.43
TIT [4]	45	111	0.10	8.6	550	0.09887	0.00071	0.014940	0.000042	0.55	0.04799	0.00029	95.60	0.27	95.73	0.65

a) Z = zircon; TIT = titanite; eq = equant; zircon treated with chemical abrasion (Mattinson, 2005), titanite not abraded

b) weight and concentrations are known to better than 10%.

c) Th/U model ratio inferred from 208/206 ratio and age of sample

d) Pbc = total common Pb in sample (initial + blank)

e) raw data, corrected for fractionation and spike

f) corrected for fractionation, spike, blank (206/204=18.59; 207/204=15.24) and initial common Pb (based on Stacey and Kramers, 1975); error calculated by propagating the main sources of uncertainty; The U-Pb ratio of the spike used for this work is adapted to 206Pb/238U = 0.015660 for the ET100 solution as obtained with the ET2535 spike at NIGL.

g) corrected for 230Th disequilibrium according to Schärer (1984) and assuming Th/U magma = 4

Forced subduction initiation recorded in the sole and crust of the Semail ophiolite, Oman

Guilmette et al.

Spot ID*	^{139}La	^{140}Ce	^{141}Pr	^{146}Nd	^{147}Sm	^{153}Eu
	in ppm					
SU03_Garnet_1	0.24	0.417	0.108	1.34	2.79	1.69
SU03_Garnet_2	0.126	0.49	0.12	1.16	1.29	0.88
SU03_Garnet_3	0.27	0.56	0.104	0.93	1.11	0.719
SU03_Garnet_4	0.28	0.49	0.09	1.09	1.13	0.96
SU03_Garnet_5	0.7	0.34	0.1	0.99	1.19	0.81
SU03_Garnet_6	0.065	0.311	0.061	0.8	1.15	0.817
SU03_Garnet_7	0.34	0.61	0.13	1.01	1.31	0.915
SU03_Garnet_8	0.074	0.37	0.3	1.42	2.08	1.101
SU03_Garnet_9	0.12	0.233	0.099	1.21	1.84	1.15
SU03_Garnet_10	0.35	0.36	0.26	1.11	1.59	0.97
SU03_Garnet_11	0.065	0.174	0.076	0.95	1.44	0.97
SU03_Garnet_12	0.05	0.197	0.073	1.16	1.4	1.074
SU03_Garnet_13	0.078	0.242	0.089	1.06	1.68	1.09
SU03_Garnet_14	0.034	0.197	0.062	1.18	1.72	1.09
SU03_Garnet_15	0.035	0.246	0.084	1.14	1.9	1.04
SU03_Garnet_16	0.152	0.273	0.086	0.96	1.61	0.991
SU03_Garnet_17	0.075	0.227	0.069	0.88	1.33	0.97
SU03_Garnet_18	0.087	0.48	0.096	1.26	1.5	1.038
SU03_Garnet_19	0.124	0.48	0.119	1.52	1.76	1.03
SU03_Garnet_20	0.21	0.426	0.149	1.84	1.64	0.942
SU03_Garnet_21	0.205	0.58	0.163	1.12	0.297	0.224
SU03_Garnet_22	0.21	0.53	0.089	0.65	0.51	0.286
SU03_Garnet_23	0.111	0.45	0.074	0.75	0.5	0.275
SU03_Garnet_24	0.127	0.44	0.084	0.76	0.57	0.407
SU03_Garnet_25	0.157	0.53	0.069	0.45	0.34	0.349

SU03_Garnet_26	0.188	0.51	0.1	0.78	0.51	0.52
SU03_Garnet_27	0.128	0.36	0.125	0.75	0.53	0.437
WT150_Garnet_1	0.06	0.29	0.044	0.43	0.71	0.495
WT150_Garnet_2	0.028	0.118	0.042	0.66	1.29	0.683
WT150_Garnet_3	0.03	0.4	0.04	0.46	0.92	0.534
WT150_Garnet_4	0.047	0.34	0.039	0.397	0.7	0.533
WT150_Garnet_5	0.036	0.083	0.038	0.396	0.77	0.551
WT150_Garnet_6	0.035	0.136	0.036	0.45	0.8	0.566
WT150_Garnet_7	0.034	0.16	0.044	0.53	0.87	0.575
WT150_Garnet_8	0.058	0.13	0.055	0.5	0.91	0.564
WT150_Garnet_9	0.074	0.305	0.066	0.54	0.81	0.536
WT150_Garnet_10	1.75	3.32	0.388	1.94	1.26	1.064
WT150_Garnet_11	0.144	0.51	0.072	0.65	0.61	0.868
WT150_Garnet_12	5.8	14.8	2	9.4	3.8	3.71
WT150_Garnet_13	0.217	0.77	0.082	0.61	0.71	0.725
WT150_Garnet_14	1.22	3.08	0.39	1.96	1.1	0.87
WT150_Garnet_15	4.3	11	1.45	7	2.62	1.8
WT150_Garnet_16	1.2	3.6	0.54	3.2	1	0.9
WT150_Garnet_17	0.201	0.79	0.086	0.57	0.79	0.675
WT150_Garnet_18	0.17	0.63	0.097	0.69	0.84	0.819
WT150_Garnet_19	1.45	4.64	0.8	3.08	1.38	0.82
WT150_Garnet_20	0.95	2.88	0.403	1.79	0.88	0.838
WT150_Garnet_21	3.04	8.4	1.21	5.9	2.62	1.49
WT150_Garnet_22	2.76	8.3	1.17	5.9	2.3	1.05
WT150_Garnet_23	0.093	0.298	0.096	0.54	0.87	0.58
WT150_Garnet_24	0.036	0.246	0.042	0.55	0.93	0.605
WT150_Garnet_25	0.036	0.171	0.029	0.46	0.92	0.564
WT150_Garnet_26	0.031	0.142	0.04	0.44	0.89	0.558
WT150_Garnet_27	0.042	0.097	0.052	0.377	0.95	0.553
WT150_Garnet_28	0.026	0.101	0.024	0.487	1.17	0.624
WT150_Garnet_29	0.013	0.104	0.046	0.57	1.11	0.673
WT-151-Garnet1	0.0198	0.106	0.039	0.51	1.01	0.624
WT-151-Garnet2	0.0068	0.077	0.043	0.94	1.71	1
WT-151-Garnet3	0.015	0.069	0.04	0.91	1.65	0.879

WT-151-Garnet4	0.0044	0.093	0.053	0.7	1.54	0.857
WT-151-Garnet5	0.023	0.164	0.05	0.81	1.68	0.96
WT-151-Garnet6	0.0013	0.052	0.024	0.46	0.62	0.47
WT-151-Garnet7	0.0024	0.039	0.0176	0.272	0.74	0.47
WT-151-Garnet8	0.013	0.037	0.0205	0.31	0.62	0.499
WT-151-Garnet9	0	0.049	0.022	0.257	0.56	0.44
WT-151-Garnet10	0.0013	0.038	0.0069	0.167	0.54	0.454
WT-151-Garnet11	0	0.032	0.014	0.215	0.54	0.5
WT-151-Garnet12	0	0.031	0.0156	0.275	0.61	0.445
WT-151-Garnet13	0.599	1.99	0.355	1.99	1.15	0.76
WT-151-Garnet14	0.0095	0.073	0.0201	0.198	0.45	0.371
WT-151-Garnet15	0.0068	0.061	0.025	0.219	0.6	0.399
WT-151-Garnet16	0	0.038	0.027	0.329	0.66	0.422
WT-151-Garnet17	0.0014	0.034	0.0179	0.238	0.65	0.506
WT-151-Garnet18	0.0013	0.029	0.025	0.25	0.51	0.464
WT-151-Garnet19	0.0029	0.02	0.0193	0.36	0.6	0.524
WT-151-Garnet20	0.43	0.045	0.0194	0.223	0.5	0.449
WT-151-Garnet21	0.0041	0.039	0.0134	0.259	0.6	0.447
WT-151-Garnet22	0.0109	0.028	0.0157	0.21	0.57	0.4
WT-151-Garnet23	0.0057	0.038	0.0159	0.186	0.39	0.382
WT-151-Garnet24	0.158	0.6	0.095	0.72	0.54	0.386
WT-151-Garnet25	0.0013	0.047	0.0136	0.241	0.46	0.461

*Analyses are georefenced in figure 4

^{157}Gd	^{159}Tb	^{163}Dy	^{165}Ho	^{166}Er	^{169}Tm	^{172}Yb	^{175}Lu
11.77	2.89	24.5	5.8	17.23	2.34	15.92	2.28
5.73	1.546	15.18	4.19	15.06	2.34	17.04	2.58
4.37	1.152	11.23	3.02	10.68	1.67	12.11	1.86
4.76	1.211	10.67	2.79	9.09	1.38	10.09	1.59
4.88	1.24	10.68	2.76	9.05	1.27	8.62	1.29
5.76	1.41	11.9	2.92	9.11	1.284	8.61	1.327
5.35	1.264	10.38	2.522	7.89	1.081	7.93	1.109
5.3	1.23	9.51	2.1	5.5	0.807	5.78	0.868
6.45	1.424	12.91	3.21	9.64	1.355	9.36	1.41
5.92	1.5	13.58	3.95	14.35	2.217	17.8	2.83
6.04	1.535	14.11	4.03	14.73	2.35	17.84	2.93
6.22	1.522	15.45	4.21	15.65	2.4	19.42	3.23
6.11	1.4	13.01	3.83	13.57	2.2	17.04	2.77
5.67	1.379	13.88	4.15	15.33	2.26	17.9	2.96
5.75	1.375	12.77	3.76	13.96	2.24	16.42	2.79
5.43	1.352	12.75	3.32	12.22	2.02	15.53	2.42
5.46	1.282	12.07	3.51	12.9	2.03	15.48	2.52
5.56	1.323	12.32	3.55	12.33	1.88	14.88	2.2
4.96	1.113	11.28	3.25	12.4	1.917	14.09	2.22
3.72	0.867	9.57	2.85	10.2	1.563	12.12	1.84
1.29	0.585	7.71	2.72	9.79	1.413	11.91	1.83
1.08	0.513	7.27	2.55	9.6	1.414	11	1.771
1.28	0.529	7.62	2.56	9.65	1.502	11.79	1.81
1.54	0.558	7.5	2.55	9.6	1.544	11.82	1.87
1.46	0.482	7.53	2.65	9.84	1.574	11.59	1.838

1.52	0.514	7.71	2.64	9.99	1.71	12.86	2.07
1.56	0.537	6.85	2.52	10.09	1.62	12.41	1.953
4.03	1.33	15.2	4.77	19	3.1	23.6	3.64
6.6	2.21	26.39	8.6	35.9	6	48.6	8.09
4.87	1.518	16.67	4.82	17.15	2.58	19.31	2.82
4.72	1.677	20.41	7.24	30.42	5.34	44.6	8.2
4.65	1.727	22.63	8.23	37.1	6.71	58.8	11.05
5.06	1.706	21.96	7.72	33.1	5.84	51.3	9.51
5.87	2.023	25.5	9.24	42.3	7.61	67.8	12.8
5.62	1.973	24.36	8.95	40.5	7.41	65.4	12.25
4.88	1.682	20.56	7.74	35.9	6.67	59.4	11.56
5.53	2.01	25.4	9.59	44.8	8.51	76.9	14.99
4.32	1.594	19.61	6.6	27.2	4.7	38.6	6.61
9.3	2.31	22.4	6.05	20.43	3.01	22.12	3.25
4.42	1.7	19.99	6.7	26.27	4.27	35	5.63
3.95	1.297	15.26	4.8	19.15	3.14	26.2	4.46
6.4	1.79	18	5.35	19.37	3.26	25.18	4
5.1	1.68	19.1	6.9	30.7	5.69	49.7	8.89
3.8	1.387	18.29	6.88	30.3	5.51	48.4	8.73
3.96	1.3	15.9	5.62	24.1	4.37	39.5	7.13
5.19	1.662	20.33	7.56	33.6	6.3	55.6	10.65
3.4	1.162	13.51	4.74	21.3	3.93	36.3	6.61
7.3	2.22	24.8	8.63	37.8	6.94	60.9	11.14
6.99	2.17	24.9	8.73	38.2	7.07	60.2	11.37
5.64	1.956	24.42	8.75	38.1	6.88	59.5	10.77
5.58	2.02	25.06	8.46	37.3	6.72	58.4	10.76
5.48	1.91	22.71	7.72	32	5.57	47.8	7.98
5.22	1.88	21.51	7.53	31.63	5.51	45.9	8.17
5.77	1.79	21.25	6.85	26.47	4.37	34.5	5.7
7.03	2.27	28.3	9.77	39.8	7.04	56.2	9.39
6.57	2.08	24.91	7.76	30.14	4.83	38	5.74
4.56	1.274	11.12	2.86	8.6	1.301	9.78	1.501
7.62	2.081	18.87	4.82	14.3	2.16	15.15	2.12
7.85	2.27	21.72	5.3	16.81	2.58	16.86	2.5

8.14	2.313	22.6	5.81	18.87	2.96	20.49	3.07
8.77	2.57	24.77	6.63	21.92	3.5	26.18	4.24
2.96	0.926	9.04	2.38	7.14	1.217	9.03	1.331
2.76	0.878	7.62	1.98	6.15	1.028	7.37	1.146
2.93	0.743	8.18	2	6.54	1.014	7.4	1.097
2.4	0.668	5.93	1.543	4.84	0.876	6.25	0.973
2.6	0.747	8.35	2.25	7.39	1.254	9	1.46
3.07	0.88	9.37	2.58	8.75	1.505	12.17	1.95
2.63	0.791	8.31	2.43	8.32	1.486	11.39	2.01
3.24	1.037	9.58	2.56	9.03	1.494	11.15	1.905
2.85	0.923	8.91	2.56	9.03	1.533	11.52	2.03
2.25	0.725	7.7	2.12	7.72	1.339	10.55	1.758
2.68	0.824	7.77	2.22	8.26	1.414	11.37	2.1
2.94	0.794	8.42	2.33	8.78	1.403	12.51	2.16
2.9	0.812	8.77	2.44	8.61	1.478	12.64	2.14
3.23	0.839	8.7	2.462	9.06	1.56	12.45	2.24
2.7	0.746	8.04	2.15	8.34	1.393	11	2.04
2.79	0.79	7.58	2.29	7.91	1.424	11.44	1.99
2.51	0.694	7.33	2.17	7.26	1.341	10.87	1.91
2.49	0.651	6.42	1.809	6.49	1.13	9.39	1.68
2.52	0.711	7.23	2.12	7.4	1.349	10.35	1.88
2.52	0.614	6.35	1.593	5.76	0.97	8.15	1.422

Yb/Dy
0.65
1.12
1.08
0.95
0.81
0.72
0.76
0.61
0.73
1.31
1.26
1.26
1.31
1.29
1.29
1.22
1.28
1.21
1.25
1.27
1.54
1.51
1.55
1.58
1.54

1.67
1.81
1.55
1.84
1.16
2.19
2.60
2.34
2.66
2.68
2.89
3.03
1.97
0.99
1.75
1.72
1.40
2.60
2.65
2.48
2.73
2.69
2.46
2.42
2.44
2.33
2.10
2.13
1.62
1.99
1.53
0.88
0.80
0.78

0.91
1.06
1.00
0.97
0.90
1.05
1.08
1.30
1.37
1.16
1.29
1.37
1.46
1.49
1.44
1.43
1.37
1.51
1.48
1.46
1.43
1.28
#DIV/0!

Forced subduction initiation recorded in the sole and crust of the Semail ophiolite, Oman

Guilmette et al.

Spot ID*	^{139}La	^{140}Ce	^{141}Pr	^{146}Nd	^{147}Sm	^{153}Eu
	in ppm					
SU03_Garnet_1	0.24	0.417	0.108	1.34	2.79	1.69
SU03_Garnet_2	0.126	0.49	0.12	1.16	1.29	0.88
SU03_Garnet_3	0.27	0.56	0.104	0.93	1.11	0.719
SU03_Garnet_4	0.28	0.49	0.09	1.09	1.13	0.96
SU03_Garnet_5	0.7	0.34	0.1	0.99	1.19	0.81
SU03_Garnet_6	0.065	0.311	0.061	0.8	1.15	0.817
SU03_Garnet_7	0.34	0.61	0.13	1.01	1.31	0.915
SU03_Garnet_8	0.074	0.37	0.3	1.42	2.08	1.101
SU03_Garnet_9	0.12	0.233	0.099	1.21	1.84	1.15
SU03_Garnet_10	0.35	0.36	0.26	1.11	1.59	0.97
SU03_Garnet_11	0.065	0.174	0.076	0.95	1.44	0.97
SU03_Garnet_12	0.05	0.197	0.073	1.16	1.4	1.074
SU03_Garnet_13	0.078	0.242	0.089	1.06	1.68	1.09
SU03_Garnet_14	0.034	0.197	0.062	1.18	1.72	1.09
SU03_Garnet_15	0.035	0.246	0.084	1.14	1.9	1.04
SU03_Garnet_16	0.152	0.273	0.086	0.96	1.61	0.991
SU03_Garnet_17	0.075	0.227	0.069	0.88	1.33	0.97
SU03_Garnet_18	0.087	0.48	0.096	1.26	1.5	1.038
SU03_Garnet_19	0.124	0.48	0.119	1.52	1.76	1.03
SU03_Garnet_20	0.21	0.426	0.149	1.84	1.64	0.942
SU03_Garnet_21	0.205	0.58	0.163	1.12	0.297	0.224
SU03_Garnet_22	0.21	0.53	0.089	0.65	0.51	0.286
SU03_Garnet_23	0.111	0.45	0.074	0.75	0.5	0.275
SU03_Garnet_24	0.127	0.44	0.084	0.76	0.57	0.407
SU03_Garnet_25	0.157	0.53	0.069	0.45	0.34	0.349

SU03_Garnet_26	0.188	0.51	0.1	0.78	0.51	0.52
SU03_Garnet_27	0.128	0.36	0.125	0.75	0.53	0.437
WT150_Garnet_1	0.06	0.29	0.044	0.43	0.71	0.495
WT150_Garnet_2	0.028	0.118	0.042	0.66	1.29	0.683
WT150_Garnet_3	0.03	0.4	0.04	0.46	0.92	0.534
WT150_Garnet_4	0.047	0.34	0.039	0.397	0.7	0.533
WT150_Garnet_5	0.036	0.083	0.038	0.396	0.77	0.551
WT150_Garnet_6	0.035	0.136	0.036	0.45	0.8	0.566
WT150_Garnet_7	0.034	0.16	0.044	0.53	0.87	0.575
WT150_Garnet_8	0.058	0.13	0.055	0.5	0.91	0.564
WT150_Garnet_9	0.074	0.305	0.066	0.54	0.81	0.536
WT150_Garnet_10	1.75	3.32	0.388	1.94	1.26	1.064
WT150_Garnet_11	0.144	0.51	0.072	0.65	0.61	0.868
WT150_Garnet_12	5.8	14.8	2	9.4	3.8	3.71
WT150_Garnet_13	0.217	0.77	0.082	0.61	0.71	0.725
WT150_Garnet_14	1.22	3.08	0.39	1.96	1.1	0.87
WT150_Garnet_15	4.3	11	1.45	7	2.62	1.8
WT150_Garnet_16	1.2	3.6	0.54	3.2	1	0.9
WT150_Garnet_17	0.201	0.79	0.086	0.57	0.79	0.675
WT150_Garnet_18	0.17	0.63	0.097	0.69	0.84	0.819
WT150_Garnet_19	1.45	4.64	0.8	3.08	1.38	0.82
WT150_Garnet_20	0.95	2.88	0.403	1.79	0.88	0.838
WT150_Garnet_21	3.04	8.4	1.21	5.9	2.62	1.49
WT150_Garnet_22	2.76	8.3	1.17	5.9	2.3	1.05
WT150_Garnet_23	0.093	0.298	0.096	0.54	0.87	0.58
WT150_Garnet_24	0.036	0.246	0.042	0.55	0.93	0.605
WT150_Garnet_25	0.036	0.171	0.029	0.46	0.92	0.564
WT150_Garnet_26	0.031	0.142	0.04	0.44	0.89	0.558
WT150_Garnet_27	0.042	0.097	0.052	0.377	0.95	0.553
WT150_Garnet_28	0.026	0.101	0.024	0.487	1.17	0.624
WT150_Garnet_29	0.013	0.104	0.046	0.57	1.11	0.673
WT-151-Garnet1	0.0198	0.106	0.039	0.51	1.01	0.624
WT-151-Garnet2	0.0068	0.077	0.043	0.94	1.71	1
WT-151-Garnet3	0.015	0.069	0.04	0.91	1.65	0.879

WT-151-Garnet4	0.0044	0.093	0.053	0.7	1.54	0.857
WT-151-Garnet5	0.023	0.164	0.05	0.81	1.68	0.96
WT-151-Garnet6	0.0013	0.052	0.024	0.46	0.62	0.47
WT-151-Garnet7	0.0024	0.039	0.0176	0.272	0.74	0.47
WT-151-Garnet8	0.013	0.037	0.0205	0.31	0.62	0.499
WT-151-Garnet9	0	0.049	0.022	0.257	0.56	0.44
WT-151-Garnet10	0.0013	0.038	0.0069	0.167	0.54	0.454
WT-151-Garnet11	0	0.032	0.014	0.215	0.54	0.5
WT-151-Garnet12	0	0.031	0.0156	0.275	0.61	0.445
WT-151-Garnet13	0.599	1.99	0.355	1.99	1.15	0.76
WT-151-Garnet14	0.0095	0.073	0.0201	0.198	0.45	0.371
WT-151-Garnet15	0.0068	0.061	0.025	0.219	0.6	0.399
WT-151-Garnet16	0	0.038	0.027	0.329	0.66	0.422
WT-151-Garnet17	0.0014	0.034	0.0179	0.238	0.65	0.506
WT-151-Garnet18	0.0013	0.029	0.025	0.25	0.51	0.464
WT-151-Garnet19	0.0029	0.02	0.0193	0.36	0.6	0.524
WT-151-Garnet20	0.43	0.045	0.0194	0.223	0.5	0.449
WT-151-Garnet21	0.0041	0.039	0.0134	0.259	0.6	0.447
WT-151-Garnet22	0.0109	0.028	0.0157	0.21	0.57	0.4
WT-151-Garnet23	0.0057	0.038	0.0159	0.186	0.39	0.382
WT-151-Garnet24	0.158	0.6	0.095	0.72	0.54	0.386
WT-151-Garnet25	0.0013	0.047	0.0136	0.241	0.46	0.461

*Analyses are georefenced in figure 4

^{157}Gd	^{159}Tb	^{163}Dy	^{165}Ho	^{166}Er	^{169}Tm	^{172}Yb	^{175}Lu
11.77	2.89	24.5	5.8	17.23	2.34	15.92	2.28
5.73	1.546	15.18	4.19	15.06	2.34	17.04	2.58
4.37	1.152	11.23	3.02	10.68	1.67	12.11	1.86
4.76	1.211	10.67	2.79	9.09	1.38	10.09	1.59
4.88	1.24	10.68	2.76	9.05	1.27	8.62	1.29
5.76	1.41	11.9	2.92	9.11	1.284	8.61	1.327
5.35	1.264	10.38	2.522	7.89	1.081	7.93	1.109
5.3	1.23	9.51	2.1	5.5	0.807	5.78	0.868
6.45	1.424	12.91	3.21	9.64	1.355	9.36	1.41
5.92	1.5	13.58	3.95	14.35	2.217	17.8	2.83
6.04	1.535	14.11	4.03	14.73	2.35	17.84	2.93
6.22	1.522	15.45	4.21	15.65	2.4	19.42	3.23
6.11	1.4	13.01	3.83	13.57	2.2	17.04	2.77
5.67	1.379	13.88	4.15	15.33	2.26	17.9	2.96
5.75	1.375	12.77	3.76	13.96	2.24	16.42	2.79
5.43	1.352	12.75	3.32	12.22	2.02	15.53	2.42
5.46	1.282	12.07	3.51	12.9	2.03	15.48	2.52
5.56	1.323	12.32	3.55	12.33	1.88	14.88	2.2
4.96	1.113	11.28	3.25	12.4	1.917	14.09	2.22
3.72	0.867	9.57	2.85	10.2	1.563	12.12	1.84
1.29	0.585	7.71	2.72	9.79	1.413	11.91	1.83
1.08	0.513	7.27	2.55	9.6	1.414	11	1.771
1.28	0.529	7.62	2.56	9.65	1.502	11.79	1.81
1.54	0.558	7.5	2.55	9.6	1.544	11.82	1.87
1.46	0.482	7.53	2.65	9.84	1.574	11.59	1.838

1.52	0.514	7.71	2.64	9.99	1.71	12.86	2.07
1.56	0.537	6.85	2.52	10.09	1.62	12.41	1.953
4.03	1.33	15.2	4.77	19	3.1	23.6	3.64
6.6	2.21	26.39	8.6	35.9	6	48.6	8.09
4.87	1.518	16.67	4.82	17.15	2.58	19.31	2.82
4.72	1.677	20.41	7.24	30.42	5.34	44.6	8.2
4.65	1.727	22.63	8.23	37.1	6.71	58.8	11.05
5.06	1.706	21.96	7.72	33.1	5.84	51.3	9.51
5.87	2.023	25.5	9.24	42.3	7.61	67.8	12.8
5.62	1.973	24.36	8.95	40.5	7.41	65.4	12.25
4.88	1.682	20.56	7.74	35.9	6.67	59.4	11.56
5.53	2.01	25.4	9.59	44.8	8.51	76.9	14.99
4.32	1.594	19.61	6.6	27.2	4.7	38.6	6.61
9.3	2.31	22.4	6.05	20.43	3.01	22.12	3.25
4.42	1.7	19.99	6.7	26.27	4.27	35	5.63
3.95	1.297	15.26	4.8	19.15	3.14	26.2	4.46
6.4	1.79	18	5.35	19.37	3.26	25.18	4
5.1	1.68	19.1	6.9	30.7	5.69	49.7	8.89
3.8	1.387	18.29	6.88	30.3	5.51	48.4	8.73
3.96	1.3	15.9	5.62	24.1	4.37	39.5	7.13
5.19	1.662	20.33	7.56	33.6	6.3	55.6	10.65
3.4	1.162	13.51	4.74	21.3	3.93	36.3	6.61
7.3	2.22	24.8	8.63	37.8	6.94	60.9	11.14
6.99	2.17	24.9	8.73	38.2	7.07	60.2	11.37
5.64	1.956	24.42	8.75	38.1	6.88	59.5	10.77
5.58	2.02	25.06	8.46	37.3	6.72	58.4	10.76
5.48	1.91	22.71	7.72	32	5.57	47.8	7.98
5.22	1.88	21.51	7.53	31.63	5.51	45.9	8.17
5.77	1.79	21.25	6.85	26.47	4.37	34.5	5.7
7.03	2.27	28.3	9.77	39.8	7.04	56.2	9.39
6.57	2.08	24.91	7.76	30.14	4.83	38	5.74
4.56	1.274	11.12	2.86	8.6	1.301	9.78	1.501
7.62	2.081	18.87	4.82	14.3	2.16	15.15	2.12
7.85	2.27	21.72	5.3	16.81	2.58	16.86	2.5

8.14	2.313	22.6	5.81	18.87	2.96	20.49	3.07
8.77	2.57	24.77	6.63	21.92	3.5	26.18	4.24
2.96	0.926	9.04	2.38	7.14	1.217	9.03	1.331
2.76	0.878	7.62	1.98	6.15	1.028	7.37	1.146
2.93	0.743	8.18	2	6.54	1.014	7.4	1.097
2.4	0.668	5.93	1.543	4.84	0.876	6.25	0.973
2.6	0.747	8.35	2.25	7.39	1.254	9	1.46
3.07	0.88	9.37	2.58	8.75	1.505	12.17	1.95
2.63	0.791	8.31	2.43	8.32	1.486	11.39	2.01
3.24	1.037	9.58	2.56	9.03	1.494	11.15	1.905
2.85	0.923	8.91	2.56	9.03	1.533	11.52	2.03
2.25	0.725	7.7	2.12	7.72	1.339	10.55	1.758
2.68	0.824	7.77	2.22	8.26	1.414	11.37	2.1
2.94	0.794	8.42	2.33	8.78	1.403	12.51	2.16
2.9	0.812	8.77	2.44	8.61	1.478	12.64	2.14
3.23	0.839	8.7	2.462	9.06	1.56	12.45	2.24
2.7	0.746	8.04	2.15	8.34	1.393	11	2.04
2.79	0.79	7.58	2.29	7.91	1.424	11.44	1.99
2.51	0.694	7.33	2.17	7.26	1.341	10.87	1.91
2.49	0.651	6.42	1.809	6.49	1.13	9.39	1.68
2.52	0.711	7.23	2.12	7.4	1.349	10.35	1.88
2.52	0.614	6.35	1.593	5.76	0.97	8.15	1.422

Yb/Dy
0.65
1.12
1.08
0.95
0.81
0.72
0.76
0.61
0.73
1.31
1.26
1.26
1.31
1.29
1.29
1.22
1.28
1.21
1.25
1.27
1.54
1.51
1.55
1.58
1.54

1.67
1.81
1.55
1.84
1.16
2.19
2.60
2.34
2.66
2.68
2.89
3.03
1.97
0.99
1.75
1.72
1.40
2.60
2.65
2.48
2.73
2.69
2.46
2.42
2.44
2.33
2.10
2.13
1.62
1.99
1.53
0.88
0.80
0.78

0.91
1.06
1.00
0.97
0.90
1.05
1.08
1.30
1.37
1.16
1.29
1.37
1.46
1.49
1.44
1.43
1.37
1.51
1.48
1.46
1.43
1.28
#DIV/0!